UC Davis

UC Davis Electronic Theses and Dissertations

Title

On the Automatic Characterization of Infrared Sensors

Permalink

https://escholarship.org/uc/item/4p0297rc

Author

Parker, Ryan Winn

Publication Date

2023

Peer reviewed|Thesis/dissertation

eScholarship.org Powered by the California Digital Library
University of California

On the Automatic Characterization of
Infrared Sensors

By

Ryan Parker

THESIS

Submitted in partial satisfaction of the requirements for the degree of

MASTER OF SCIENCE

in

Electrical and Computer Engineering

in the

OFFICE OF GRADUATE STUDIES

of the

UNIVERSITY OF CALIFORNIA
DAVIS

Approved:

Juan Sebastian Gomez Diaz

Diego Yankelevich

William Putnam

Committee in Charge

2023

On the Automatic Characterization of Infrared Sensors

Ryan Parker
rwparker@ucdavis.edu
Electrical and Computer Engineering Department, University of California Davis, USA
Supervised by: Dr. J. S. Gomez-Diaz
jsgomez@ucdavis.edu
Electrical and Computer Engineering Department, University of California Davis, USA

***Abstract*—Testing the next generation of novel infrared sensors in a research setting can be a time-consuming and expensive procedure. To address this challenge, an automated solution for characterizing miniaturized optical sensing devices is presented. The system enables rapid, automated characterization of thousands of miniaturized devices. The advantages of this system include its low cost, high flexibility, and speed. It enables fast and unique statistical analysis to determine performance and optimal design parameters by individually testing thousands of devices. The proposed system uses a single microprobe to individually test and characterize thousands of devices using optical and RF interrogation techniques, individually spending 20 seconds on each sequential device. Without any need for human input the system allows for the collection of massive amounts of data. Furthermore, the system can easily adapt to different device types, chip layouts and light sources. It uses a precision 2D stage retrofitted with open-source electro-mechanical hardware and software to allow accessibility to any chip. This versatile system can be employed to characterize a wide variety of different devices. Experimentally, the system successfully characterized thousands of meta-surface enhanced aluminum nitride contour mode MEMS resonators. The figures of merit evaluated in the experiments include quality factor, fluctuation-induced noise, responsivity, and noise equivalent power. The best device observed was a detector with a calculated noise equivalent power (NEP) of 80 pW/$\sqrt{\mathrm{Hz}}$; for this device, the quality factor, responsivity, and fluctuation noise spectral density was found to be 2531, 300 Hz/nW, and 0.37 Hz/$\sqrt{\mathrm{Hz}}$. Overall, this automated system offers an efficient and cost-effective solution for characterizing the next generation of miniaturized optical sensing devices. It provides researchers with a powerful tool for data collection and analysis, enabling quick advancements in the development of IR sensors.**

***Index Terms*—IR, automation, sensors, MEMS, NEMS, characterization, measurement.**

I. Introduction

INFRARED (IR) devices play a vital role in the future of sensing. IR sensors are integral to various aspects of our lives. Infrared detectors importantly play a critical role in national Security. United States Air Force Colonel George B. Hept claims that IR technology has been a "chaotic evolution that has successfully influenced the state of air operations" [1]. IR sensors are employed in military equipment for targeting and optics systems. IR sensors played a chaotic role in the 1979 Soviet-Afghan war where the CIA armed the Mujahideen Muslim freedom fighters with small, IR guided portable Surface-to-Air Missiles to fight the Soviet army's air force. It was a great success and played a pivotal role in the conflict. Other air-to-air missiles such as the sidewinder and python were developed with the same technology that allowed users to "fire and forget". IR systems are also used for military vision and targeting. Since the 1960s the United States air force has been involved in the research of IR detectors [2]. In Desert Storm in the Persian Gulf, IR systems were used very successfully to engage enemy armour at night and in dust storms. Military aircraft such as A-10 Warthogs and F-15 Eagles were retrofitted with IR based vision and targeting systems that played a critical role in this conflict [1]. IR technology is also used in space telescopes like the James Webb space telescope which operates with two different IR detectors for wide-band sensing capability. By utilizing a mercury-cadmium telluride detector as well as an arsenic-doped silicon detector, detection in the range of 0.5 μm - 28 μm is possible [3]. Additionally, they are used for spectroscopy (i.e., Fourier Transform IR spectroscopy, FTIR) which finds multiple applications to analyze chemical components in samples such as pollen [4] or cancer [5]. Given their significance in enhancing system capabilities, there is a growing need to expedite the development of infrared devices.

Before the advent of narrowband semiconductor alloys such as the widely used II–VI ($Hg_{1-x}Cd_xTe$), the first infrared detectors were built on polycrystalline lead salt. Since then, the advent of photo-lithography and advanced nano-machining has greatly expanded the different types on infrared detectors available, such as thermopiles, bolometers, pyroelectric detectors, and even exotic detectors like cantilevers and golay cells [2], [6]. IR sensor development has become a large and diverse field, but the development of the next generation of infrared sensing devices faces a significant bottleneck due to the traditionally slow development methods [7], [8]. In terms of characterization, dicing, and wirebonding, significant time is required, hindering overall testing throughput. Although some advanced micro-probe stations can automate the measurement of dies, they are prohibitively expensive and may not be compatible with optical sensors. Furthermore, custom micro-probe cards are often required for each novel design and chip layout. Research labs necessitate a flexible and affordable automated testing system capable of accommodating both RF and IR interrogation techniques without compromising throughput.

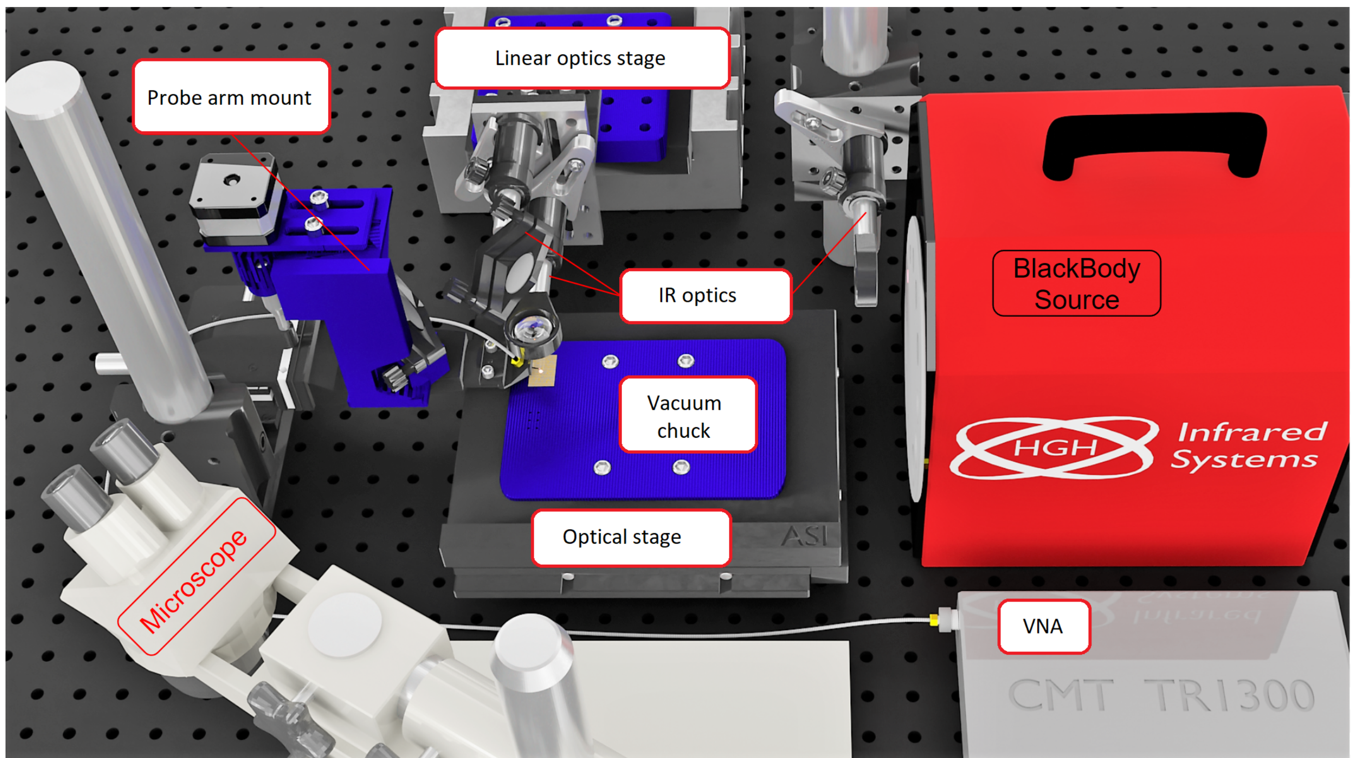

Fig. 1. The proposed IR characterization system comprises a high precision XY stage, a micro-probe arm with a 3D printed motor mount, a vector network analyzer (VNA), a blackbody source, and an optics assembly on a linear stage. The linear optics stage holds the optical path to focus IR radiation onto the sample at the micro-probe tip. A vacuum chuck is bolted to the stage to secure the chip under test. The VNA connects to the micro-probe arm for RF characterization of the samples. The microscope is used to align the chip and perform the first initial landing.

In this paper, I present a cost-effective automated characterization system that will allow the characterization thousands of novel IR sensor devices per chip. The goal of this system is to provide researchers the ability to characterize thousands of devices in terms of RF quality factor, responsivity, fluctuation induced noise, and noise equivalent power. The proposed system is pictured in figure 1. It incorporates a blackbody radiator, a retractable optical path, a precision motorized sample stage, and a custom automated microprobe arm. This system implements highly flexible testing methods that can be adapted to a wide variety of different devices. Analysis of the data produced by the system yields wafermaps, device trends, and statistics that can be analyzed along with design parameters such as anchor dimensions, thermal resistance, and more. Statistics can be extracted from the data allowing for the discovery of the optimal device parameters for the highest quality devices.

This technology goes beyond the state-of-the-art because it incorporates many different aspects of testing with automation. Some of the aspects of this system have been developed independently elsewhere, but it has not been combined and implemented with such testing throughput. As silicon photonic systems progress, photonic integrated circuits (PIC) emerge from the laboratory into to foundries. High-throughput testing systems for devices based on this technology exist, but do not allow for the wide-band IR characterization and RF testing of novel IR sensors. However, current methods primarily involve the use of clamped fiber couples for optical interrogation, rather than incident IR radiation. While some existing systems, as mentioned in references [9] and [10], demonstrate automated RF and IR characterization capabilities using microprobes and optical fiber interconnects, they only work with devices that use a clamped optical fiber for optical testing. Similarly, reference [11] showcases a promising system by GlobalFoundries, focused on RF/DC testing, but it relies on fiber waveguides that may not be suitable for IR sensors. Therefore, a flexible dedicated IR measurement system is needed for novel state-of-the-art sensors. Preliminary steps towards this direction have been reported in reference [12]. Although this system enables RF and optical interrogation at cryogenic temperatures even, it lacks the necessary throughput that automation can achieve. While automated sample positioning has been demonstrated in IR device characterization systems, as exemplified in reference [13], this work combines aspects of automation and optical interrogation to allow the automated testing of optical interconnects, but does not allow the RF characterization or infrared interrogation.

To demonstrate the system performance, chips with thousands of state-of-the-art lateral countour mode resonator (CMR) aluminum nitride micro-electromechanical systems (MEMS) loaded with spectrally selective IR metasurfaces are tested. A SEM image of a specific sensor is shown in figure 2. These novel devices are infrared sensors that sense subtle temperature variations in the bulk of the resonator. The resonator itself floats micrometers above the substrate, suspended by two anchors. The metasurfaces that cover the

resonators are made of arrays of specially designed crosses or patches whose IR absorption spectra are verified with a Bruker FTIR microscope. These novel devices operate in a unique way. The sensors absorb heat in a narrowband of absorbance determined by the metasurface. The heating of the bulk of the resonator causes a shift in the resonant frequency of the device due to the thermal coefficient of the aluminum nitride. The physical dimensions of the device, the Young's modulus, and the piezoelectric coefficient all affect the resonant frequency [14], [15], [16].

What makes these devices so unique is the response of the device is in the form of a frequency shift that must be detected by other electrical equipment. The responsivity of these devices can defined as a frequency shift of the MEMS RF resonance divided by the incident radiation power causing the shift or as by the phase change of the device divided by the power causing the shift. In this paper, the responsivity in terms of frequency is going to be investigated. Figures of merit for these devices are quality factor, fluctuation-induced noise, responsivity, time constant, and noise equivalent power (NEP) [2]. In this case, the blackbody radiation and the metasurface absorption play a crucial role to find the in-band radiation power contributing to the shift. The NEP is calculated from the fluctuation induced noise and the responsivity. In our test, thousands of sensors located on a 3 cm by 5 cm chip are tested. The dimensions of the entire chip are roughly 3 cm by 5 cm. Of the measured metrics, the highest quality factor was 2800, the highest responsivity was 2 Hz/nW, the lowest fluctuation induced noise was 0.256 $\mathrm{Hz}/\sqrt{\mathrm{Hz}}$, and the lowest NEP was 80 $\mathrm{pW}/\sqrt{\mathrm{Hz}}$.

This paper is organized as following. Section II will describe the system hardware and components. Section III will discuss the characterization procedure of the devices and the metrics involved with characterizing the novel MEMS IR sensors. Section IV details the operational procedure of the automated measurement system. Section V discusses the results and statistics of the thousands of measured devices. Section VI concludes with a discussion of the challenges overcome and potential future modifications.

II. System Description

The proposed IR system is designed to land a single microprobe on thousands of devices, and test each device individually with RF and optical methods before saving the data and moving on to the the next device. To achieve this, the IR characterization setup is composed of a precision motorized XY translation stage that holds the sample under test, a motorized micro-probe arm, a blackbody radiator, and a linear stage holding the infrared optical path. This setup is shown in figure 1. On the optical stage, a 3D printed vacuum chuck is employed to securely hold the chip in place. The optical components can be moved in or out of the beam path by the linear stage, allowing control over the incident radiation on the device at the micro-probe tip. In the following, an overview of the parts of the system is presented.

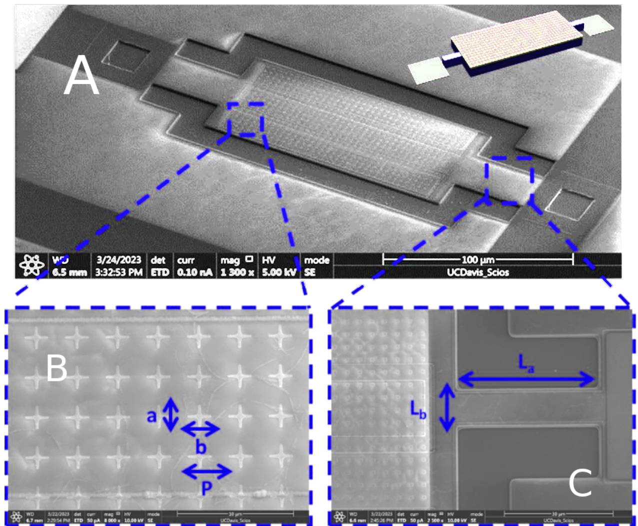

Fig. 2. A: A 200MHz aluminum nitride CMR MEMS resonator with metasurface before back-etching. B: The tunable parameters for the metasurface are shown for a cross type metasurface. C: The tunable parameters for the resonator anchors are shown on a CMR MEMS with a patch type metasurface.

A. 2D Optical Stage

The stage that moves the sample must be very precise. An ASI MS-2000 stage is used and has positional repeatability less than 1 μm, and features closed-loop feedback for precise positioning and a serial interface for remote automation. The stage is mounted on another 3D printed part for mounting directly to an optical table. The stage does not include any mounting holes, so a 3D-printed vacuum chuck was designed and secured to the stage.

B. Vacuum Chuck

The vacuum chuck provides a flat surface with small holes that adheres the chip securely when low vacuum is applied. A vacuum chuck is necessary to keep the chip stationary on the stage during probing, and a dedicated one has been fabricated for this system. Specifically, the vacuum chuck comprises two 3D-printed plates that bolt together sandwiching the top layer of the ASI stage. As shown in figure 3, the top plate features a grid of small holes connected to a network of small tunnels inside the vacuum chuck, each with a diameter of 3 mm. These tunnels lead to a small outlet port on the back of the vacuum chuck. At the outlet port, a small vacuum pump provides the suction necessary to secure the sample to the chuck for probing. Two sample locations are available, one for a sample and one for a calibration substrate. By connecting the vacuum pump to this outlet port, the negative pressure required to secure the chips to the stage is provided.

Designing and constructing the vacuum chuck was a challenge as the ASI XY translation stage did not have any mounting points. While some commercial products may have more robust construction, they are also large, bulky, heavy, lack flexibility, and cannot be customized. For the custom chuck to work well, the chuck's surface must be exceptionally flat and smooth. This can be achieved by printing Polylactic acid (PLA) filament on a flat glass bed [17]. When using

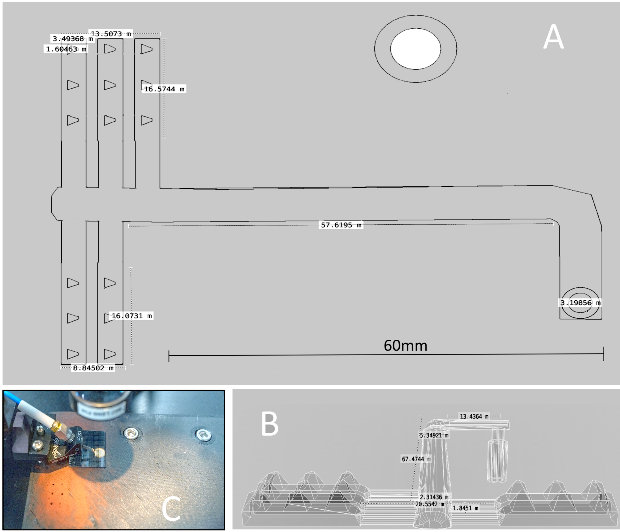

Fig. 3. A: A top down orthographic view of the somewhat triangular holes and the tunnel system that provides suction to the bottom of the chip. Dimensions are supplied for the embedded lines in the print. The tunnel diameter varies from 2.5 mm to 1.5 mm. Two different mounting points are supplied for sample and calibration substrate. B: A 3-dimensional rendering of the tunnel system and its corresponding dimensions. C: A picture of the physical chuck. The print material is ABS mixed with 15% chopped carbon fiber. The orange color is a rubber sealant that has been polished into the surface.

this approach, the bottom layer (the chuck surface) melts against the glass, filling in any cracks left from normal plastic extrusion. Without a glass bed, the ridges on the surface will cause air leakage and poor vacuum adhesion. Alternatively, polishing the surface with sealant can allow the use of strong filaments such as carbon-fiber ABS or nylon can be used. The polishing is necessary for these higher temperature filaments because the filament extrusions leave gaps in the surface that do not melt together.

C. Blackbody Radiator and IR Optics

For the sensors tested in this thesis, blackbody radiation is used as the IR source, but any IR source can be easily adapted for use within the proposed system. The blackbody radiator is a HGH model CRN1350. It is capable of heating to 1350 °C and has multiple different aperture sizes that can be used. Up to 25 mW of power can be delivered to the sample in a 2 mm diameter by varying the blackbody temperature. Figure 4 illustrates the spectral irradiance of the blackbody radiator at different temperatures, following Planck's blackbody law. The source has emissivity greater than 0.99 after calibration. The temperature stability is 0.1 °C, and the temperature accuracy is less than 2 °C [18]. The spatial beam profile and power level of the system is characterized. This is done by scanning a small Mercury-Cadmium-Telluride sensor (Thorlabs PDAVJ10) on the ASI XY translation stage and rastering an image of the focused spatial IR radiation from the sensor data using a lock-in amplifier and a chopper [19]. The PDAVJ10 sensor has an active area of 1 mm by 1 mm. This radiation profile is used to determine the power that is reaching each device [20]. Figure 5 shows the spatial profile of the blackbody radiator.

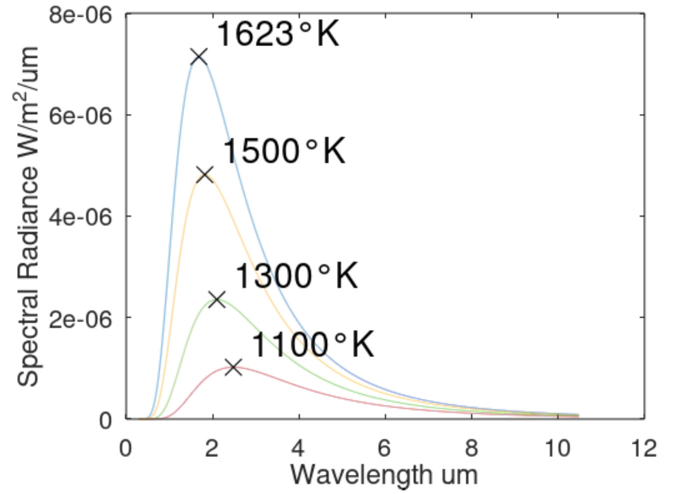

Fig. 4. The spectral profiles of the HGH RCN1350 blackbody radiator irradiance for different temperatures.

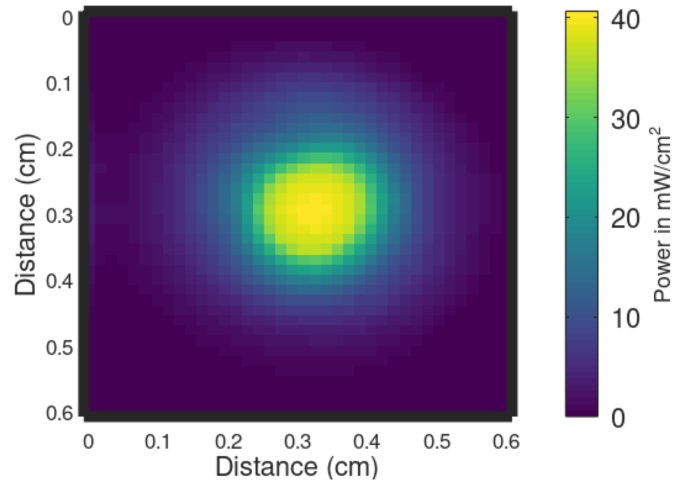

Fig. 5. The focused blackbody radiation beam profile incident on the device taken by scanning a Thorlabs PDAVJ10 infrared detector with the ASI stage. Chopped IR radiation was used as a source, and a lock-in amplifier was used to measure the signal from the detector.

To provide the IR light to the devices, a linear stage is used to move the optical path components in and out of the correct place. In this experiment, static IR radiation is compared to background radiation of the lab, which was kept low with dimmers. The linear stage is a one dimensional stage where the optical components are mounted. It is pictured here in figure 6. The optics are mounted at a 90 degree angle, such that the post assemblies are horizontal. After exiting the blackbody and passing through the first collimating optic, the horizontal mirror directs the collimated blackbody radiation downward. Below the mirror is a Barium Fluoride focusing lens that focuses the IR light onto the micro-probe tip. As the light is focused to the micro-probe tip, when the micro-probe lands on a new device, the IR radiation remains focused on each device. The focusing optics utilized are Ekspla wide-band BaF_2 lenses [21] and gold mirrors. The whole optical assembly is mounted on a small 3D printed optical table

made from sturdy carbon-fiber nylon material. This allows for many different optical components to be mounted on the stage and allows control over the incidence of IR radiation on the sample. The high precision linear stage can move the optical components in or out of the beam path of the blackbody with micrometer precision. When retracted, the stage moves far enough to prevent any IR from reaching the sample. The linear stage movements take about 15 seconds. The linear stage is an Anorad model 91842 that comes with its own proprietary controller. It runs on five volt current-based transistor logic and utilizes optical isolators at its input. The current output from a Teensy 4.0 micro-controller is less than 5 mA per pin and less than 25 mA for all pins. For compatibility with a low current CMOS based micro-controller, a high-side npn common-emitter amplifier is used. The amplifier limits the current draw from the micro-controller and is able to source large amounts of current to the controller's opto-isolators. In this configuration, the npn is used as a high-side switch preventing full voltage output, but this is not necessary in this case as only the opto-isolator LED needs to be energized to send the signal which only requires sufficient current once biased.

D. Micro-Probe Arm

A standard 150 μm GSG 40A micro-probe is used to make electrical connection with the devices. To automate the landing, 3D printed parts are used to significantly enhance the stage and micro-probe arm. The micro-probe arm is augmented with a motor for driving the micro-probe landing and a mirror positioned directly above the micro-probe to help focus laser radiation. Electrical testing is performed automatically with a vector network analyzer (VNA) connected to the micro-probe.

To test many devices automatically, the micro-probe must be landed correctly and carefully. To automate the micro-probe arm, 3D printed parts were designed to couple a stepper motor to the z axis adjustment knob of the micro-probe arm. There are three printed parts that are used to do this as illustrated in figure 8. Part one bolts directly to the arm of the micro-probe station and features an additional mirror mount. Part two, which is what holds the stepper to the top of part one, has a notch that slides in a groove on the top of part one. This allows for fine positioning and adjustment to make sure the axes are lined up. Part three couples the motor to the micro-probe arm adjustment knob. The shaft of the motor fits snug inside the printed part, which took a few iterations for tolerances to be perfect. A screw is used to tighten against the motor shaft and prevent any slip. For the micro-probe arm, a layer of electrical or masking tape is used to ensure a snug fit and again secured with a screw. A mirror mount that is incorporated into the micro-probe arm and allows for laser radiation to be reflected into the optical path of the linear stage when it is moved into the beam path. In this way, the system can be operated with focused blackbody radiation or laser radiation. The stepper mount allows for the coupling of a NEMA 17 stepper motor to the vertical adjustment knob of the micro-probe arm. The printed part directly bolts onto the micro-probe arm. The motor couple is made with two separate parts that mesh with fingers. This design allows for axial slip. On this specific micro-probe arm, the micro-probe arm and motor mount moves while the adjustment knob stays in the same position, it is necessary for the motor mount to have some vertical slack to move independently from the knob.

E. Electro-Mechanical Control

To properly operate the system, the micro-probe landing is initially done manually while viewing with a microscope. By landing the micro-probe manually and then energizing the motor, the system starts in the landed position. The system knows how far to land because it started in a landed position and was retracted a known amount. By retracting the micro-probe a known amount, it is able to land again automatically by landing the same amount that was initially retracted.

The micro-controller controls both the linear stage and the micro-probe arm stepper motors with a stepper controller library called *SpeedyStepper* [22]. This library allows for precise control of the acceleration and position of both stepper motors. It was found that the maximum speed of stepper motor operation is highly dependent on the clock frequency of the microprocessor for this library. The teensy 4.0 has a dual core, 32 bit, ARM cortex M7 processor with a clock speed of 600 MHz and executes two instructions per cycle about 40% of the time based on profiled Arduino code [23]. This speed was entirely necessary for the quick movement of the stage. Operation of the stage with a generic Arduino resulted in linear stage movements that took over 2 minutes per cycle. The micro-probe arm and linear stage automation are achieved using a stepper motor controller commonly employed in 3D printers as well as custom firmware. The system uses a Texas Instruments DRV8825 stepper controller for smooth control of the micro-probe arm motor, and a proprietary Anorad controller for precise and fast control of the linear stage. The electrical connections for the microcontroller and the motor controllers are shown in figure 9. Since the micro-probe arm stepper motor operates with no feedback, so it is imperative that the rotation of the knob is smooth. If any steps are missed due to any frictional force that overcomes the motor's torque, the micro-probe may fail to land properly. Lubrication is important for any old micro-probe arms to ensures smooth, correct operation.

The Teensy 4.0 interfaces with both motor controllers as well as a personal computer via a virtual serial port over USB. The computer is also interfacing with the VNA over a local TCP connection created by the VNA software, enabling the transmission of measurement commands and data. Communication between the computer and microcontroller occurs through a serial interface, allowing for the transmission of movement commands for both the linear stage and the micro-probe arm. Another serial connection is established between the computer and the ASI XY translation stage to send movement commands and receive position data. Prior to testing, the location data of the devices must be extracted from the photomask and incorporated into the Matlab program's memory. The devices can be arranged in an array with constant offsets to simplify the measurement algorithm. The entire

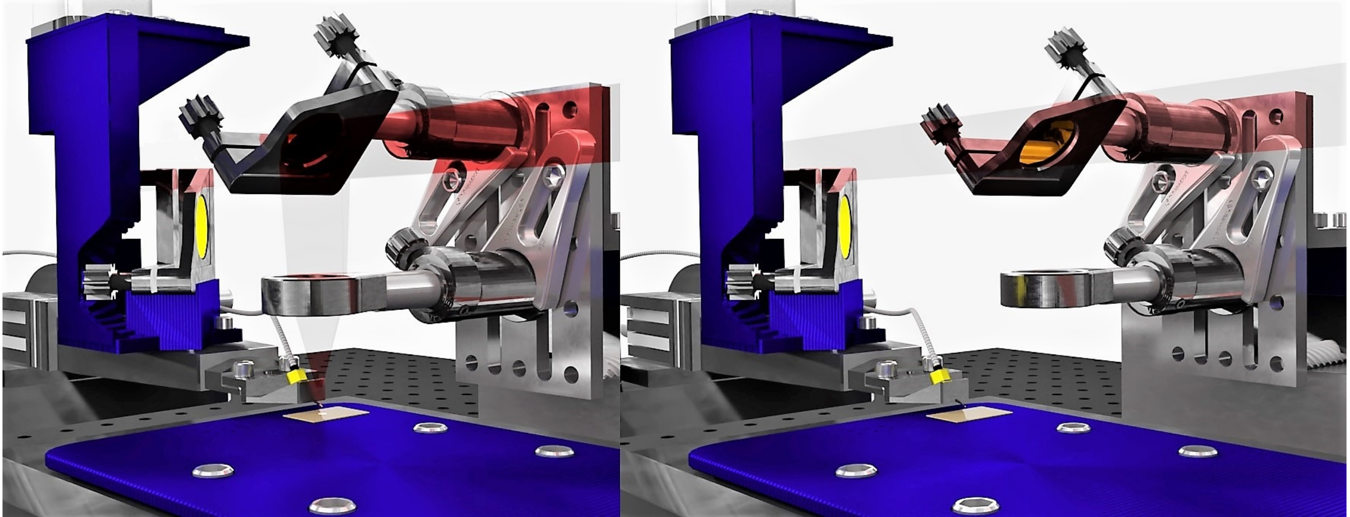

Fig. 6. A rendering of the automated micro-probe station with optical path components inserted (left panel) and retracted (right panel) via the linear stage.

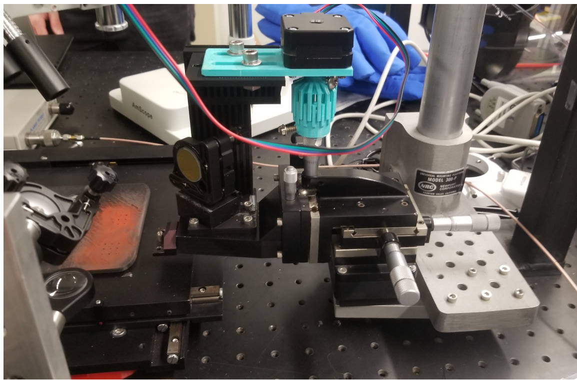

Fig. 7. Picture of the constructed automated probe arm.

system is controlled by a home-made Matlab program, which coordinates and synchronizes the actions of the optical stage, linear stage, and motorized micro-probe arm, and VNA.

To interface with the Matlab program that runs the system, a simple serial interface protocol was devised for the microcontroller. The first byte of a message would enumerate the command. Most movement commands are a single byte; they inform the microcontroller to move the micro-probe up or down a predetermined amount, or to move the linear stage forward or backward a predetermined amount. The automation code and a microcontroller unit (MCU) firmware incorporates redundancy to ensure that the system knows when the micro-probe or stage has completed its movement to prevent micro-probe damage. For linear stage move commands and micro-probe move commands, only 1 byte of data is sent to the MCU at a time. Upon receiving the data, the MCU performs the associated action and sends an acknowledgement byte in response. Until receiving the acknowledgement command, the Matlab program pauses. Upon receiving the acknowledgment, it will proceed. This ensures only a single movement occurs at a time, keeping the micro-probe from being damaged. Redundancy is also incorporated in stage movement commands as well. For translation stage movement commands, a movement command

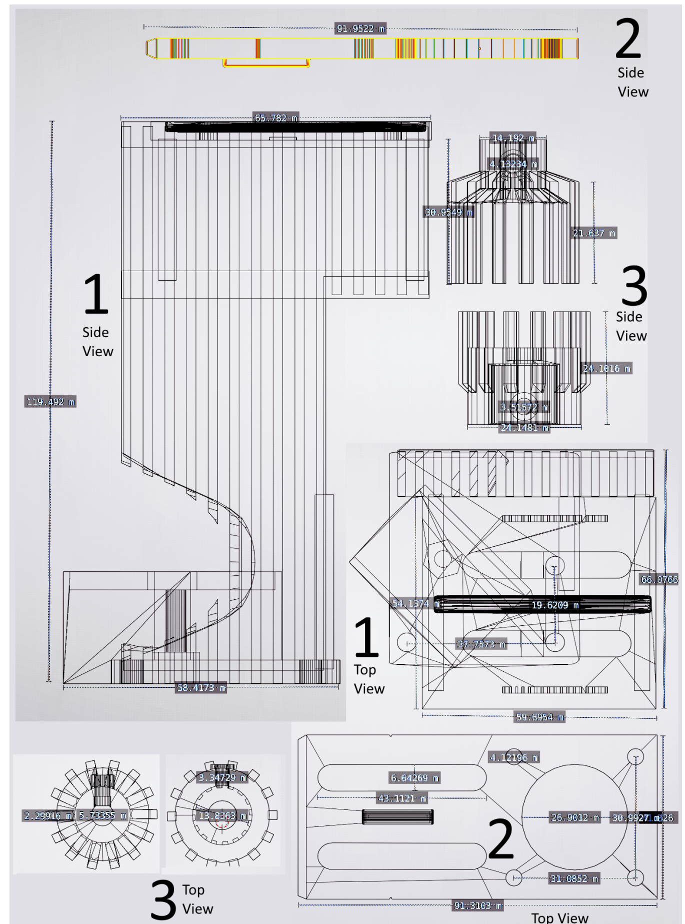

Fig. 8. This diagram shows the dimensions of the printed parts that couple the motor to the micro-probe arm shaft and mount the motor to the micro-probe arm itself. Part one is the main body of the mount, It secures to the probe arm and holds a mirror. On top of part one sits part two. This parts is where the NEMA 17 stepper motor bolts to. Part two has a central oblong protrusion running lengthwise that fits in a groove of part one. The two long holes give lots of flexiblity for mounting and fine adjustments to the alignment of the shaft coupler. Part three is actually two individual parts that mesh together with fingers. They secure to the stepper motor shaft and the vertical adjustment knob of the micro-probe arm. Each part is pictured with multiple angles, each labeled.

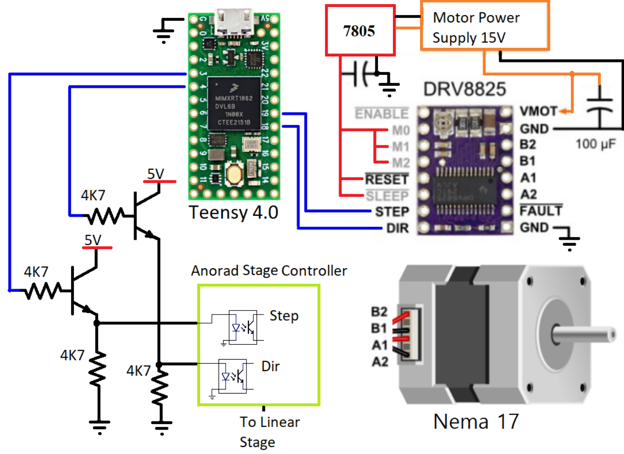

Fig. 9. A diagram of the electrical connections of the microcontroller and stepper controllers. Here a high-performance microprocessor is responsible for the precision movement of the micro-probe and optical assembly.

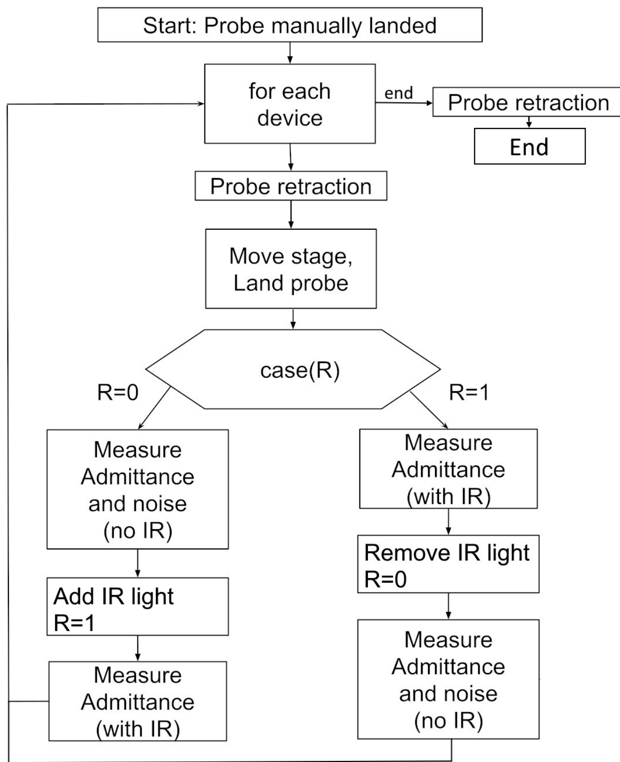

Fig. 10. The system control loop diagram demonstrates the measurement algorithm and time optimization, only moving the linear stage once per device.

includes the move keyword as well as the XY coordinates to move to. Once a movement command is sent, the Matlab program polls the stage controller, requesting the position of the stage. Once the stage had traversed at least 98% of the travel distance, the Matlab function for stage movement returns and the Matlab program proceeds.

F. RF characterization

The RF characterization of each device is performed automatically through a loopback TCP/IP interface on the host computer created by the VNA software. A Coppermountain technology planar TR1300/1 VNA is used. The Matlab program interfaces with the VNA software which allows the sending of commands and the receiving of data to and from the VNA via USB. Initially the VNA is calibrated on a bandwidth where most normal responses are expected. Since all devices tested are one port devices, the VNA is calibrated with a GGB CS-8 callibration substrate on short, open, and load. During testing, the VNA measures the S_{11} admittance parameter and converts it to Y_{11} parameter. This measurement is done with and without IR light to see any static response. Chopped IR light can also be used. An example of the code used to interface with the VNA is included in the appendix.

Figure 10 illustrates the optimal testing procedure for speed, where only one linear stage move is performed per device. In this diagram, the boolean variable "R" represents the position of the stage, indicating whether IR radiation is provided to the device. The system moves the stage and the micro-probe to each device in the chip in order to test each one sequentially. The stage, micro-probe arm, and optical path are all moved with careful precision and redundancy. The VNA facilitates the RF testing when the micro-probe is in a landed state.

III. Characterization Procedure

The goal of the characterization is to find performance metrics of the fabricated devices, such as quality factor, noise spectral density, responsivity, noise equivalent power, and time constant. In this case, the devices are CMR MEMS resonators patterned with spectrally selective IR metasurfaces as shown in figure 2. These IR detectors operate by heat from in-band incident IR radiation causing a shift in the resonant frequency of the device. In the next subsections, the different measurement procedures will be discussed for extracting the figures of merit for the tested devices. These sections are quality factor, fluctuation induced noise, NEP, and time constant.

A. Quality Factor

The quality factor is defined as the fractional bandwidth of the resonator, and is proportional to the ratio of energy stored by the resonator to the energy dissipated by the resonator in each cycle. This metric is intrinsic to the performance of these devices. High quality devices will, by definition, have a sharper resonance. Since these devices operate by detecting temperature change with a shift in the resonant frequency, higher quality resonators will allow smaller shifts to be detected more easily, giving a higher performance detector [25],[24]. The quality factor of each device is found automatically by the Matlab program. The Y_{11} admittance parameter data received from the VNA are three vectors, frequency, phase, and log-magnitude. From the log-magnitude and frequency vectors, the quality factor is extracted by finding the two points that are 3dB below the maximum of the resonance peak on either side. The admittance magnitude plot is shown in figure 12 along with the shift caused by incident blackbody radiation. The highest performing CMR MEMS device with metasurface had a quality factor of 2800. After measuring the admittance,

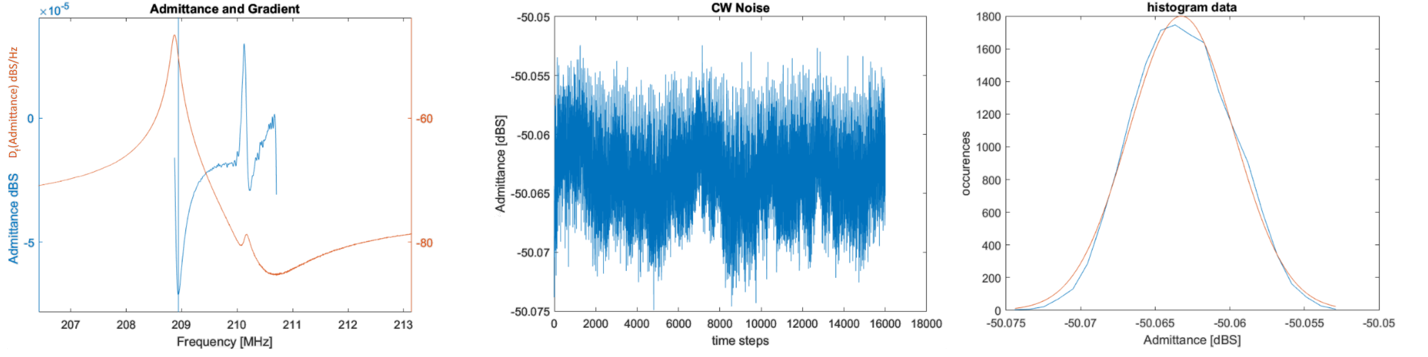

Fig. 11. Left: The admittance and its derivative are plotted to find the high-slope point. Middle: The CW time-domain measurement at the high slope point. Right: The RMS frequency noise spectral density is estimated by curve fitting a gaussian to the distribution of the data in an automated process using a VNA. By exciting the resonators at the high slope point, the frequency fluctuations are converted to admittance fluctuations and are measured statistically using thousands of samples.

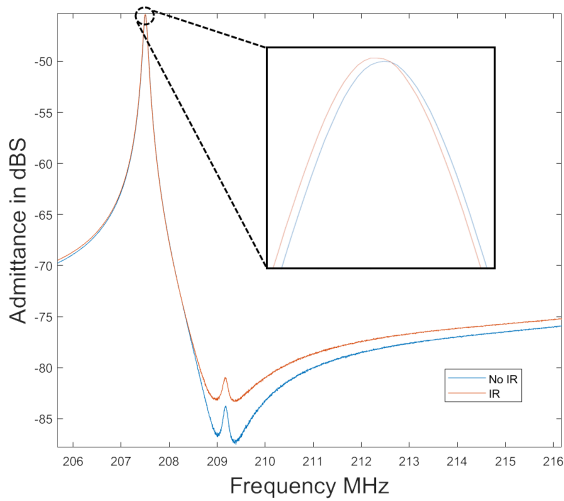

Fig. 12. A single admittance measurement of a 200MHz CMR MEMS resonator with metasurface

a technique used to estimate fluctuation induced noise is performed.

B. Fluctuation Induced Noise

The fluctuation induced noise of each resonator represents the noise associated with the sensor and is an estimation of the noise spectral density of the detector. A lower noise is of course more desirable as it means the noise floor is lower and the signal to noise ratio will be higher. The noise associated with these sensors is measured in units of Hz/$\sqrt{\text{Hz}}$ since the heating of the sensor causes a frequency shift. Thermal, mechanical, and RF noise sources are encountered in these devices which all contribute to its overall noise. To quantify the fluctuation induced noise, an automated VNA measurement process is devised. Once the micro-probe lands on a device without any IR light, and the admittance parameter is measured, the Matlab algorithm finds the point of highest (negative) slope on the resonator curve between the parallel and series resonances. The VNA is then set for single-tone or continuous wave (CW) excitation at this high-slope frequency. At this point the VNA is only measuring a single frequency, so each measurement is just a collection of measurement at the same frequency separated only in time. At a rate of 10 KHz, 16,001 samples are taken; an example of this measurement is shown in the center plot of figure 11. Finally the standard deviation of the samples are taken. A histogram of the data is also curve fit to a gaussian for calculation of the R squared fit factor. The RMS frequency noise spectral density is found by dividing the standard deviation of the single-tone admittance samples by the slope of the admittance curve and the square-root of the IF bandwidth of the VNA. This formula is shown in equation 1:

$$f_n = \frac{\sigma_Y}{\frac{dY}{df}(f_s)\sqrt{B_W}} \tag{1}$$

Here sigma represents the standard deviation of the CW admittance at the high slope point, B_W represents the measurement bandwidth, and $\frac{dY}{df}(f_s)$ represents the slope of the admittance curve at the high slope point f_s A similar method was published in reference [15]. The VNA is then reset to the original frequency range for the testing of subsequent devices. This method may be susceptible to random sources of noise and large perturbations in the RF response of the device. This was a problem in the system that led to the generation of a significant number of outliers in the noise measurements of different devices. The lowest noise device measured was 0.256 Hz/$\sqrt{\text{Hz}}$ which is state-of-the-art compared to previous reported fluctuation induced noise of measurement of 1.46 Hz/$\sqrt{\text{Hz}}$ [15] and 1.0 Hz/$\sqrt{\text{Hz}}$ [26] .

To validate this method of noise measurement, the same MEMS sensor devices are measured with a Keysight e5052b phase noise measurement tool. To measure the phase noise of the devices, a resonator is constructed from the devices using a directional coupler, low-noise amplifier, and phase delay. A diagram of the resonator is pictured in figure 13. The resonator configuration allows the MEMS resonator to entertain a stable state of oscillation that incorporates the noise from the device. Since the detection of incident IR is found from deviations in the resonant frequency, this method gives a good estimation of the noise that will be encountered in an actual detector. The output of this oscillator is taken to the Keysight e5052b signal source analyzer with a power splitter. The phase noise measurement was converted to frequency

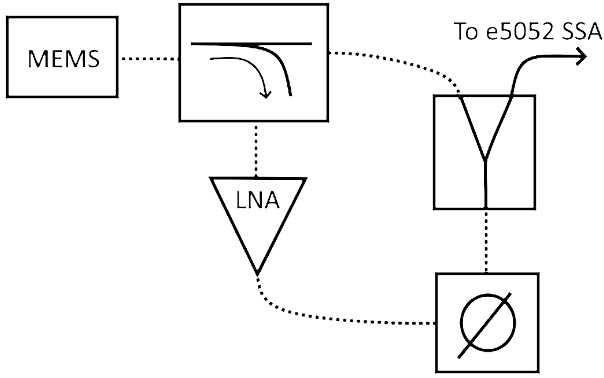

Fig. 13. This RF diagram shows the construction of the resonator from a one port MEMS sensor devices. Here a directional coupler isolates reflections from the MEMS which are amplified, delayed, and applied back to the MEMS device. A Keysight e5052b signal source analyzer analyzes the signal.

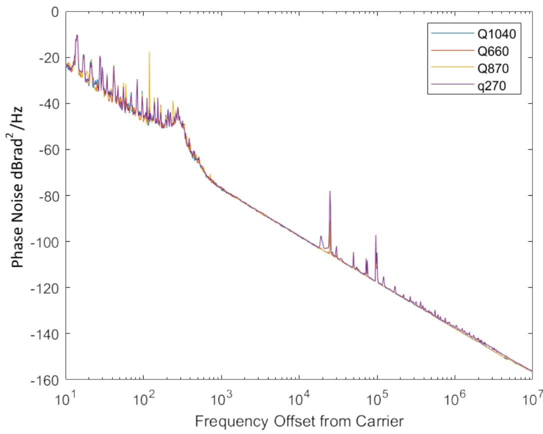

Fig. 14. A plot of a phase noise measurement of several resonators taken by the Keysight e5052b is shown. The frequency noise spectral density of the devices between 10Hz and 100Hz is computed to be 0.23 Hz/$\sqrt{\text{Hz}}$ which is 0.15 Hz/$\sqrt{\text{Hz}}$ less than the average noise measurement of the same devices with the VNA. The lack in noise variation with devices indicates that the noise performance of the device is dependent on the system exciting it.

noise and compared to the noise measured by the VNA. The phase noise spectral density measurement is plotted in figure 14. The signal source analyzer found a noise spectral density that was about 50% lower than the average of the same devices measured with the VNA in the offset frequency range between 10 Hz and 200 Hz. Multiple devices are plotted showing little variation in the noise measurement. The noise of the devices is indistinguishable from the noise from the rest of the resonator.

C. *Responsivity*

The responsivity of a device is the magnitude of the devices frequency shift to incident IR radiation. For these devices, the responsivity is measured in Hz/W. This unit corresponds the the frequency shift due to the in-band power that caused it. To test the responsivity of the IR sensors, the devices are measured with no incident IR radiation and with a constant IR illumination from a blackbody radiator. This is done by measuring the admittance parameter of the device once without IR illumination and once with IR illumination. The responsivity of devices is found from the frequency shift due to the IR radiation power absorbed by the metasurface of each device. This absorbed power is dependent on the surface area of the device, the spectral absorbance of the metasurface, and the power spectral density of the IR radiation impinging on the devices. Figure 15 shows some spectral absorption profiles for some metasurfaces that were patterened on the devices (see fig. 2b). To find the incident in-band power on the device, the spatial distribution of the blackbody radiation is integrated over the area of the detector and the spectral power distribution is integrated with the absorbance of the metasurfaces. Unfortunately not all metasurfaces were measured, so one metasurface from each tile containing a unique metasurface was measured and used for each device in that tile. This constitutes an excellent approximation because all metasurfaces in each tile are identical, but we will see in the results that a manufacturing process error caused some variation in devices. Equation 2 shows how the responsivity is calculated:

$$R_V = \frac{f_s}{A \int E(\lambda) M(\lambda) d\lambda} \tag{2}$$

Here, A is the sensor area, E(λ) is the blackbody spectral irradiance, M(λ) is the metasurface absorption spectrum, and f_s is the frequency shift measured from the IR radiation.

To find the responsivity, the frequency difference of the peak admittance point with and without IR radiation is measured. This frequency shift is divided by the incident power in the absorption band of the metasurface on the device to find the responsivity in Hz/W as shown in equation 2 [27]. To find the power in the absorption band of the metasurface, the spectral profile of the incident IR irradiance is multiplied by the spectral absorption of the metasurface before integrating and multiplying by the area of the device. To calculate this, the metasurface absorption spectrum must be multiplied by the blackbody radiation spectrum and integrated. The Matlab program does this by processing Bruker FTIR microscope measurement data from a single device from each tile. For

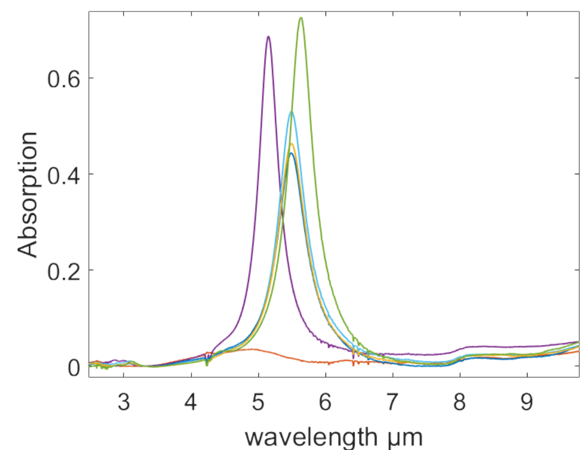

Fig. 15. FTIR measurements of different 200 MHz CMR MEMS with metasurfaces.

the best performing device, the measured responsivity was 400 Hz/nW, which is significantly higher than the previous recorded responsivity of 0.68 Hz/nW in [15] and 0.53 Hz/nW in [26].

D. Noise Equivalent Power

NEP is one of the most important metrics in characterizing a sensor as it quantifies the sensitivity of the device. The NEP is defined as the radiant IR power that produces a signal equal to the noise level at a specified bandwidth and wavelength of the system [28]. For these devices, the NEP is calculated by dividing the noise spectral density by the sensitivity. This is shown in equation 3:

$$NEP = \frac{f_n}{R_v} \tag{3}$$

Two previous papers on these devices have shown experimental NEPs of 1.9 nW/$\sqrt{\text{Hz}}$ [26] and 2.1 nW/$\sqrt{\text{Hz}}$. The NEP of the best performing device is 80 pW/$\sqrt{\text{Hz}}$, which is state-of-the-art considering the previous studies on these devices. Considering hundreds of the top performing devices, the NEP is on average 350 pW/$\sqrt{\text{Hz}}$.

E. Time Constant

The time constant of a sensor is an important metric to quantify the speed that a detector can respond to a stimulus. It can measured as the time required to reach 63.2% of its full output from a step input. It can also be measured by finding the chopper frequency that causes a 3dB attenuation in the response. To measure the time constant of these devices two methods are applied. The first method finds the time that is taken to reach 63.2% of its output. The second method analyzes responses from different frequencies of chopped IR excitation to find the 3dB point. The response of the device to chopped IR radiation is measured across different chopping frequencies and a curve is fit to the data to find the time constant. By varying the speed of a chopper, the time constant can be deduced by measuring the attenuation of the response relative to chopper frequency. The expected temperature response of the IR detector is shown in equation 4 [26].

$$\delta T = \frac{\eta Q_p}{\sqrt{G_{th}^2 + \omega^2 C_{th}^2}} \tag{4}$$

In this equation, η is the metasurface absorption, Q_p is the incident power, G_{th} is the thermal conductance of the device to the substrate, C_{th} is the thermal capacitance of the device, and ω is the chopper frequency modulating the IR radiation.

To measure the response of the devices to alternating stimulus, a similar method as the noise measurement method is used as follows. After measuring the admittance parameter spectrum of a device, the VNA is set to a single-tone, CW mode at the high slope point of the device. With the chopper IR light incident on the device, time-domain measurements are collected for varying chopper frequencies. For the first method, the rise time is directly taken from this data, giving a result of 700 μs. For the second method, the VNA is used

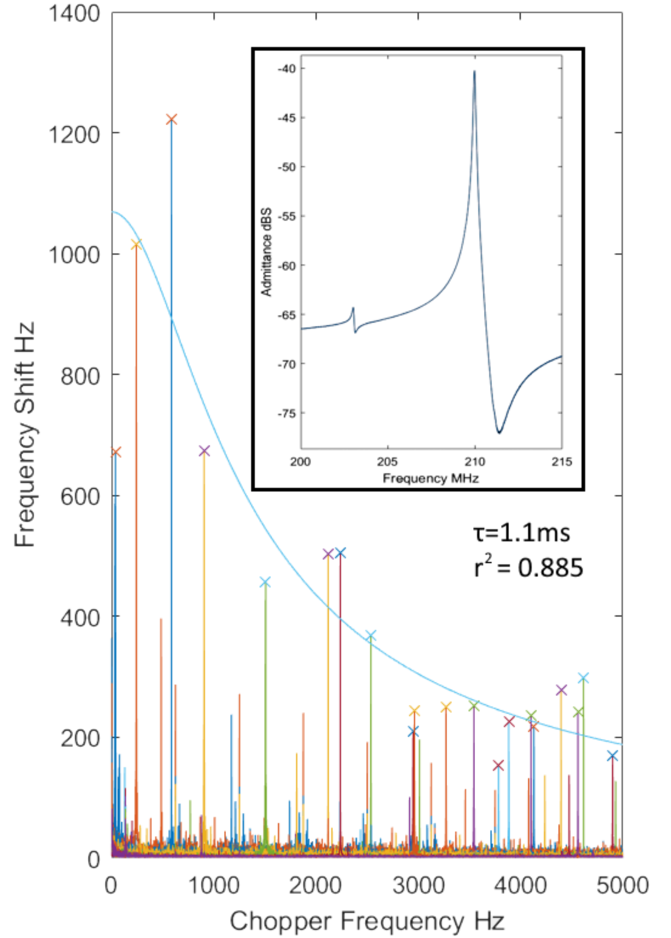

Fig. 16. After measuring the device admittance pictured in the top right, the time constant of the IR detectors is found using single-tone excitation with the VNA. Multiple time domain CW measurements are processed in the frequency domain to find the primary harmonic of the chopper and the magnitude of its response. This is performed for many chopper frequencies; each 'x' marks the spot of these maximums. In Matlab a low-pass filter is curve fit to these points to find the time constant as well as the thermal resistance and thermal capacitance.

to take time-domain data which is analyzed in the frequency domain in Matlab. At a 10KHz IF bandwidth, a sample is taken every 100 μs. At this rate, chopping speeds up to 5 KHz can be supported. To find the time constant, many VNA measurements are taken and processed digitally in Matlab to find the amplitude of response and chopping frequency. To process each measurement, the Fourier transform of each time-domain measurement is taken. The strongest harmonic detected is isolated and the magnitude and frequency is extracted. This process is performed on all the measurements until many samples of admittance amplitude versus chopper frequency are collected. Curve fitting techniques are used to fit a low-pass filter to the data. This process was not automated in this paper, but it is possible to automate with the techniques described here if the chopper speed can be controlled digitally. An example of this process is shown in figure 16.

IV. System Setup and Operation

In order to measure thousands of devices automatically with the system, a few things must be done to initialize

it correctly. The spatial power distribution of the blackbody radiation reaching the sensor must be measured. The chip and calibration substrate are loaded onto the stage and aligned correctly on the vacuum chuck. The VNA is calibrated with a CS5 calibration substrate. A short-open-load procedure is used as all the devices are one port. Then the microprobe is moved to the location where the IR light will illuminate the tip and each device the probe lands on for testing. The stage is moved so the probe is in the correct starting position on the chip, and the origin of the ASI stage is set. Then the microscope illuminator can be extinguished and the automated probing can begin.

A naming convention is a necessity when dealing with such large amounts of device measurements. The Matlab program will guide the stage and the micro-probe to land on each device. It will save admittance measurements from each of the devices and then perform a noise measurement and save that as well. An example of a single device's admittance measurement is shown in figure 12. Once the probing is complete, the micro-probe is retracted extra high and the data can be processed and analyzed to get all of the figures of merit for each device. The autonomous testing rate of the system is around 15 seconds per device. Additionally, about an hour is taken to setup the system.

To characterize many sensors located on the same chip, an algorithm must be devised to generate the position of each device that is to be tested. This is done by extracting location data from the photomask. For the chip tested in this paper, approximately 2,835 CMR MEMS resonators are fabricated on a chip. Each chip has a 3x7 array of tiles containing 135 devices. Each tile, pictured in figure 17, has the same devices, the only difference being different metasurface patterns targeting different wavelengths in the mid-IR spectrum. Each tile position has a device with the same exact design parameters for the physical MEMS resonator. The tiles are spaced consistently and each contain a 15x9 array of devices. They rows of the 15x9 array is evenly spaced, but the column spacing is dependent on device size to some extent and is non-uniform. Therefore, all the individual horizontal distances between the device columns must be recorded in a array of 14 horizontal offsets. The distance between rows is simply a scalar since they are all the same. Each device inside of a tile can be found by summing the offsets based on the row and column of the device. Two nested for-loops simply iterate two variables from 1-9 and 1-15. The same thing happens for the tiles. The horizontal and vertical distances between the tiles are constant. So the final algorithm for measuring all devices results in four nested for-loops as seen in the code segment included in the appendix.

After the testing procedure and algorithm is devised, and the photomask data is processed into the necessary data to guide the stage, the infrared optics need to be aligned. This is done with a thermal image sensor or IR detector cards. Once the IR is focused to the tip of the probe, the IR optics can be retracted and a microscope can be used to calibrate the VNA. Then the chip is placed on the vacuum chuck and secured with vacuum. Once the chip is secured and roughly in the right position, the chuck must be leveled. This is only necessary for the 3D

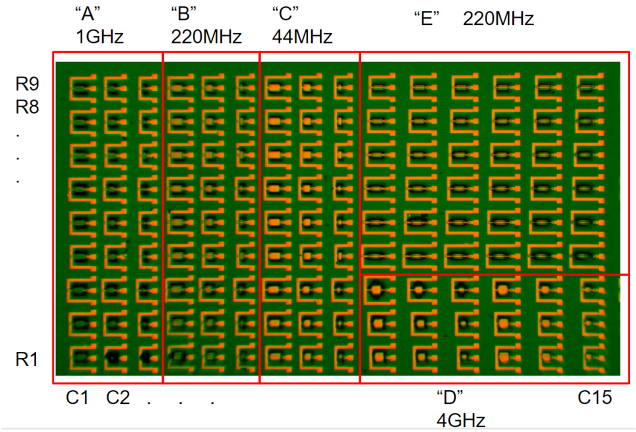

Fig. 17. This is the device layout of a single tile. The tiling is repeated on the chip 21 times in a three by seven grid. Each tile has the same unique metasurface patterned on all devices in the tile.

printed chuck and only needs to be done after installation. The leveling of the chuck can be done by tensioning the four bolts that secure the chuck to the stage. Verification of the flatness of the chuck is done by scanning the microscope across the sample and verifying the focus of the microscope is maintained. Additionally, the micro-probe can be landed at three or four points on the sample and the horizontal displacement of the micro-probe can be measured visually to ensure proper flatness of the chuck. Finally, an alignment procedure is performed to ensure the chip is properly oriented with the axes of the stage. This can be accomplished visually by moving the stage in a straight line across the chip and visually checking the movement of the micro-probe relative to the devices in a column. If the micro-probe does not follow the devices in a straight line, but instead deviates left or right, then an angular correction is applied to the chip by manually rotating the chip with the vacuum temporarily suspended. This process is repeated until the chip is properly aligned with the axes of the stage. When this happens the XY translation stage will be able to accurately find any device and initiate a micro-probe landing. The required angular tolerances depend on the device pad size and the overall chip size. For the chip tested in this paper, a deviation of less than 0.5 degrees is necessary. Although this task can be time-consuming, once achieved, it allows for the automatic measurement of all devices on the chip.

V. Results

For this section the measuremets from a single chip containing over 2000 measured devices will be summarized. The measurements that are taken by the automated measurement system result in many different useful device metrics. By utilizing all available data in performing device analysis, relations between quality factor, thermal resistance, noise can be explored. Design parameters such as photomask data, thermal resistance data, and anchor dimensions are not measured directly but can still be incorporated into an insightful analysis. Quality factor, noise, and responsivity are all directly measured and can be correlated with design parameters such as thermal

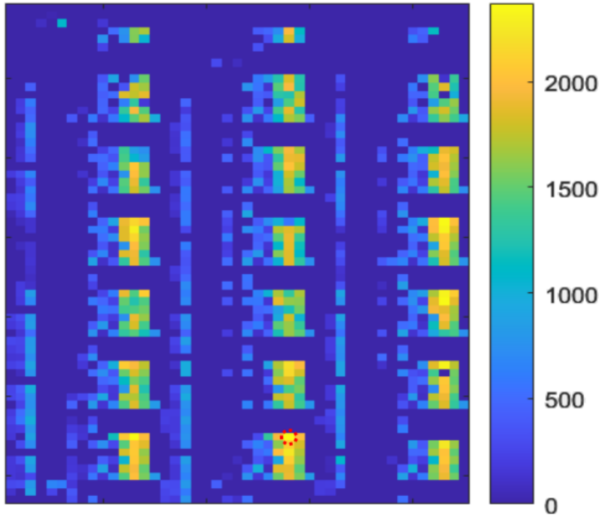

Fig. 18. This spatial heat map of device performance is colored by resonator quality factor. This diagram clearly shows the high performance of the 200MHz 'E'CMR MEMS devices, which are focused highly in the analysis of the devices.

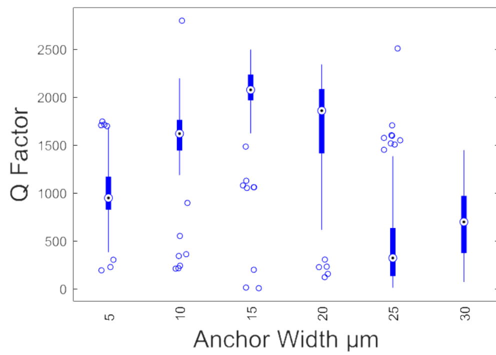

Fig. 19. The average quality factor versus anchor width is plotted for 'E' devices.

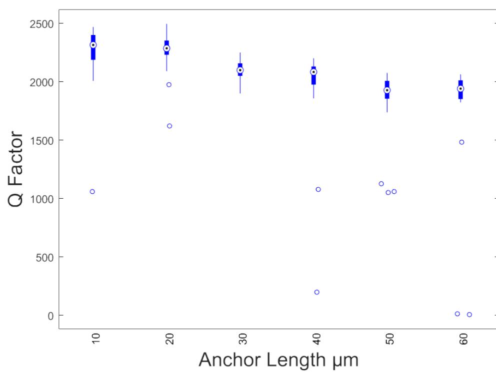

Fig. 20. The average Q factor is plotted for all anchors of width 15 μm for 'E' 200MHz CMR MEMS devices

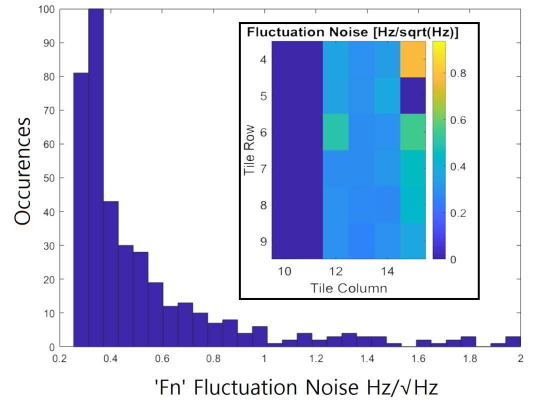

Fig. 21. The integrated frequency noise distribution of all 200MHz CMR MEMS devices are plotted in a histogram. The noise characterisation method is described in section 3B.

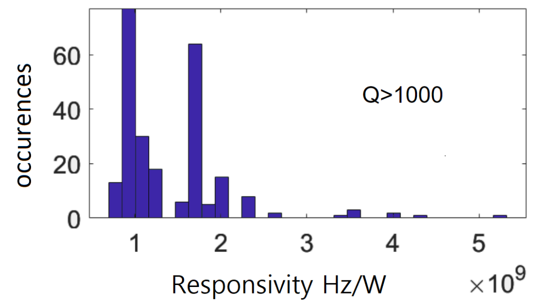

Fig. 22. The responsivity distribution of 200MHz CMR MEMS devices is plotted in a histogram. The responsivity is measured using the frequency shift and incident in-band power absorbed.

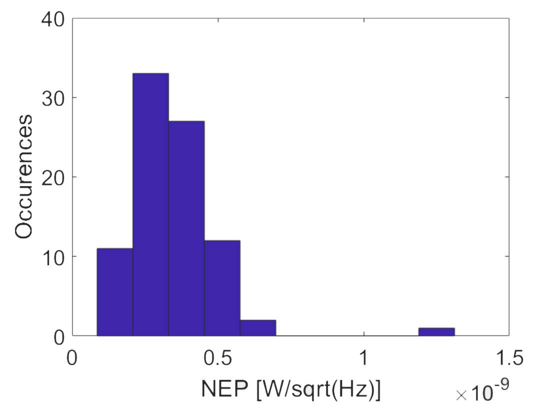

Fig. 23. The NEP distribution of 200MHz CMR MEMS devices is plotted in a histogram.

resistance and anchor dimensions. The automated measurement system renders hundreds of thousands of datapoints in the form of admittance and time domain measurements that require complex processing techniques. The processing of the data is performed by a Matlab program that processes the data from each device as well as other external data sources such as FTIR data and noise measurements. The output of the data process generates many different forms of useful data.

Shown in figure 18 is a spatial plot of device quality factor. Here, each pixel is a device whose color represents its quality factor. Similar to commercial wafer level test facilities, this system can produce spatial plots of different device parameters called 'wafer maps' or in this case 'chip maps'. Our top performing device is circled with a dotted red line. From this, one can quickly get a sense of which devices were top performing out of the thousands of devices that were measured. It is then also possible to elucidate the optimal design parameters such as geometric dimensions of the top devices. It is evident that the 200 MHz devices, from which our top performing device was selected, are performing with very high quality factors. These devices were focused on specifically for further analysis in terms of quality factor, responsivity, noise, and NEP.

In figure 19 and figure 20, device quality factor is plotted in a bar graph versus anchor dimensions of width and length (see fig. 2). This graph shows that an anchor width of 15 μm is clearly optimal. Figure 20 plots all of the quality factors of devices with 15 μm wide anchors versus anchor length, the optimal width shown in figure 19. Both figures show the optimal anchor dimensions for these devices with this process is 15 μm and 10 μm-20 μm for anchor width and length respectively.

Fluctuation induced noise data is also produced by the system. The fluctuation noise distribution plotted in figure 21 shows an average of 0.35 Hz/$\sqrt{\text{Hz}}$ with the best noise performance at 0.256 Hz/$\sqrt{\text{Hz}}$. The best noise performance was the same devices with high quality factor. The noise of these devices is state-of-the-art compared to previous reported fluctuation induced noise measurement of 1.46 Hz/$\sqrt{\text{Hz}}$ [15] and one Hz/$\sqrt{\text{Hz}}$ [26]. The dimensions of the anchors of the lowest noise and highest Q devices were 10 μm long and 15 μm wide.

The responsivity measured by the system was also very high. The highest responsivity measured by the system was 2 Hz/nW while the average responsivity was 1.43 Hz/nW. These results are an improvement over previous work's recorded responsivity measurements of 0.68 Hz/nW in [15] and 0.53 Hz/nW in [26].

The NEP distribution is pictured in figure 23. The lowest NEP measured was 80 pW/$\sqrt{\text{Hz}}$ while the average was 350 pW/$\sqrt{\text{Hz}}$. These NEP measurements are signifigantly better than previous works NEP meausrements of 1.9 nW/$\sqrt{\text{Hz}}$ [26] and 2.1 nW/$\sqrt{\text{Hz}}$.

Due to the large amount of data that can be collected by the system, interesting relationships between thermal resistance, noise, and quality factor can be found. Figure 24 shows a plot of hundreds of valid fluctuation noise measurements, each from individual devices. The data forms two asymptotes, one of which is a vertical asymptote at a quality factor of 750 and the other is a horizontal asymptote at a frequency noise of 0.35 Hz/$\sqrt{\text{Hz}}$. The vertical asymptote is an artifact of the testing algorithm. It was deemed unnecessary to measure the noise of devices with quality factors less than 800. The horizontal asymptote seems to be a noise floor. This noise floor is most likely due to frequency noise of the VNA. Figure 25 shows a plot of the quality factor versus thermal resistance. The thermal resistance of the MEMS resonators is almost entirely dictated by the anchor dimensions. From Leeson's equation, phase noise and quality factor are inversely proportional [29].

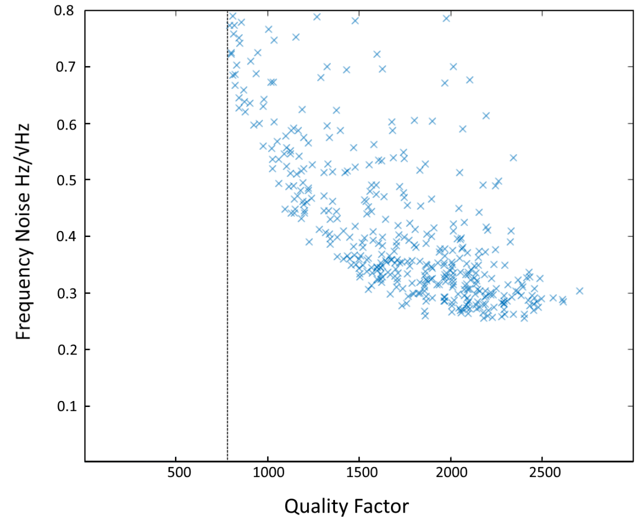

Fig. 24. This plot shows the measurements of the noise of each device versus the quality factor. Here each point is an individual device. The vertical line represents the quality value cutoff for noise analysis. Any devices with quality factor below 750 were not analyzed in terms of noise.

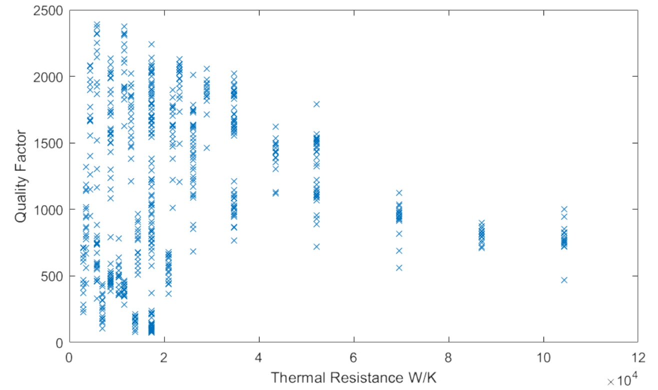

Fig. 25. This plot shows the quality factor of each device versus the thermal resistance. Here each point is an individual device.

VI. Conclusion

The automated system presented in this paper was extremely useful in the testing and characterization of the novel, state-of-the-art CMR MEMS IR sensors. This unique work demonstrates the use of automation and IR device characterization to harvest vast amount of data on thousands of devices. With

this tool, sensor parameter enumeration and optimization is possible allowing for the rapid development of novel devices.

There were many challenges faced during the development of this project, and there are some improvements that can be implemented to further enhance the performance of the proposed system. First, the noise measurement algorithm is quite sensitive to vibration, light, and other noise sources. Many data points deemed outliers were culled from the dataset. A remedy for this issue is to perform multiple noise measurements and take the lowest one. This will only increase testing time for a second or two per device. Second, many of the different data for responsivity are missing. The responsivity data in figure 22 is lacking much data because there were some issues with the XY translation stage. Some of the data was taken in two different probings of the same device, and there were landing accuracy errors on the second time around. This explains why the amount of data is less than what is measured. The XY translation stage used was a 16 years old model and was only meant for use as a proof of concept. A very precise translation stage is required for this to continuously work. The stage must be capable of reliably landing with sub-μm precision. When using such a motorized stage, it may be advisable to set limitations on acceleration, deceleration, and velocity to reduce wear on the precision components. Third, the bimodal distribution in the responsivity of figure 22 is attributed to a metasurface absorption issue. The issue stems from a planarization problem in the manufacturing process. After the deposition of the gold fingers on top of the aluminum nitride bulk, a thin film of silicon dioxide layer is deposited that conformed to the ridges of the electrodes. Due to the valleys of the surface on which they were built, the metasurfaces failed to perform at peak efficiency. In fact, the automated measurement system was instrumental in discovering this issue. Fourth and finally, the NEP data shown in figure 23 has even less data since both the noise data and the responsivity data is required for each device to calculate its NEP. If the noise or responsivity data was not found due to probing error or random noise, the NEP for that device could not be found or was an outlier. Despite this the NEP data for the top performing devices is very impressive. The measured devices here are working very well, but there is no reason to stop here. Higher quality factors may still be achieved through the use of phononic crystals. There is very interesting work on buffing the quality factor of these resonators by augmenting the anchors with phononic crystals [30], [31], [32], [33].

The most recent version of this system incorporates all measurements in a single landing, and a new fabrication process is being developed to planarize the MEMS devices before patterning the metasurface. Future work will certainly involve the characterization of responsivity in terms of phase and admittance variation. In this paper, Y_{11} admittance parameter magnitude is considered, but additional response can be found from the phase as well. In this way, two responsivities can be defined for each phase and magnitude. Using a VNA, responsivities in the order of 6.4 $^{\circ}/\mu$W have been measured in these devices, but were not characterized en masse. Methods to improve resilience in noise measurement include performing the same measurement multiple times and averaging or taking the best one. The biggest issue encountered in the development process was the loss of accuracy in the old ASI stage. During this project, a beryllium copper micro-probe was used to land on over 10,000 devices before its retirement. Although this is extremely impressive lifespan for a probe, the landing quality deteriorates as the micro-probe wears. Tungsten tipped probes are recommended for this system as they are more robust than beryllium copper and can withstand more abuse. Additionally, a large issue becomes debris; as probing is conducted, bits of dust or even flakes of metal from the landing pads can become lodged in the micro-probe and require cleaning. Performing probing in a clean room is a huge benefit as it can prevent data loss and needless wear on microprobes if the measurements are not monitored. A great method is to monitor the probing remotely. Additionally, a simple and worth-wile improvement would be the addition of a rotation stage to the XY motorized translation stage. Operating the vacuum chuck on top of this would speed up the process of alignment and greatly improve the user experience.

In conclusion, the automated measurement system is very useful for the characterization and development of novel optical sensors. This system provides valuable characteristics of thousands of optical sensors while remaining open-source and cost-effective. Demonstrated is the characterization of thousands of state-of-the-art MEMS IR detectors and the profiling of optimal design parameters. This technology is very accessible for any lab to use and can save hundreds of thousands of dollars in proprietary equipment and man-hours of work.

References

[1] G. Hept, Infrared Systems for Tactical Aviation: An Evolution in Military Affairs, United States: Air war coll maxwell afb al, 2002.

[2] A. Rogalski, Infrared Detectors, 2nd ed. CRC Press, 2010, pp. 33–40.

[3] Rieke, G. H. (2007). Infrared detector arrays for astronomy. In R. Blandford, J. Kormendy, and E. Dishoeck (Eds.), Annual Review of Astronomy and Astrophysics (pp. 77 to 115). (Annual Review of Astronomy and Astrophysics; Vol. 45). https://doi.org/10.1146/annurev.astro.44.051905.092436

[4] Kendel Adriana, Zimmermann Boris, Chemical Analysis of Pollen by FT-Raman and FTIR Spectroscopies, Frontiers in Plant Science vol.11, 2020, 10.3389/fpls.2020.00352

[5] Su KY, Lee WL. Fourier Transform Infrared Spectroscopy as a Cancer Screening and Diagnostic Tool: A Review and Prospects. Cancers (Basel). 2020 Jan 1;12(1):115. doi: 10.3390/cancers12010115. PMID: 31906324; PMCID: PMC7017192.

[6] S. Huang, H. Tao, I. -K. Lin and X. Zhang, "Double-Cantilever Infrared Detector: Fabrication, Curvature Control and Demonstration of Thermal Detection," TRANSDUCERS 2007 - 2007 International Solid-State Sensors, Actuators and Microsystems Conference, Lyon, France, 2007, pp. 1601-1604, doi: 10.1109/SENSOR.2007.4300454.

[7] S. J. PI, "Conquering the Silicon Photonics Production Bottleneck," www.photonics.com. (accessed Jul. 08, 2023).

[8] Scott Jordan, "Automating Photonic Alignment Addresses Silicon Photonics Production Bottleneck," US Tech Online, www.us-tech.com. (accessed Jul. 08, 2023).

[9] Zhang, Peng, et al. "Test system for wafer-level silicon-photonics testing." Optical Design and Testing X. Vol. 11548. SPIE, 2020.

[10] Flores, Jaime Gonzalo Flor, et al. "AtOMICS: A neural network-based Automated Optomechanical Intelligent Coupling System for testing and characterization of silicon photonics chiplets." arXiv preprint arXiv:2210.16946 (2022).

[11] A. Aboketaf, C. Hedges, V. Dhurgude, B. Harris, F. Guan, F. Pavlik, T. Anderson, A. Stricker, Y. Bian, M. Rakowski, A. Dasgupta, and A. Paganini, ”Towards fully automated testing and characterization for photonic compact modeling on 300-mm wafer platform,” in Optical Fiber Communication Conference (OFC) 2021, P. Dong, J. Kani, C. Xie, R. Casellas, C. Cole, and M. Li, eds., OSA Technical Digest (Optica Publishing Group, 2021), paper W6A.1.

[12] Giessmann, Sebastian, and Frank-Michael Werner. ”Wafer level test solutions for IR sensors.” Infrared Imaging Systems: Design, Analysis, Modeling, and Testing XXV. Vol. 9071. SPIE, 2014.

[13] Rong Zhang and F. G. Shi, ”Manufacturing of laser diode modules: Integration and automation of laser diode-fiber alignment and RIN characterization,” in IEEE Transactions on Advanced Packaging, vol. 26, no. 2, pp. 128-132, May 2003, doi: 10.1109/TADVP.2003.817473.

[14] Kang, S., Qian, Z., Rajaram, V., Calisgan, S. D., Alù, A., Rinaldi, M., Advanced Optical Materials 2019, 7, 1801236. https://doi.org/10.1002/adom.201801236

[15] Hui, Yu I& Gomez-Diaz, Juan I& Qian, Zhenyun I& Alù, Andrea I& Rinaldi, Matteo. (2016). Plasmonic piezoelectric nanomechanical resonator for spectrally selective infrared sensing. Nature Communications. 7. 11249. 10.1038/ncomms11249.

[16] Jung, JY., Song, K., Choi, JH. et al. Infrared broadband metasurface absorber for reducing the thermal mass of a microbolometer. Sci Rep 7, 430 (2017). https://doi.org/10.1038/s41598-017-00586-x

[17] Bandar Abdullah Aloyaydi, Subbarayan Sivasankaran, Hany Rizk Ammar. Influence of infill density on microstructure and flexural behavior of 3D printed PLA thermoplastic parts processed by fusion deposition modeling[J]. AIMS Materials Science, 2019, 6(6): 1033-1048. doi: 10.3934/matersci.2019.6.1033

[18] “RCN series - high temperature cavity blackbody,” HGH Infrared USA, https://hgh-infrared-usa.com/rcn-series/ (accessed Jun. 9, 2023).

[19] “Thorlabs - PDAVJ10 HgCdTe Amplified Photodetector, 2.0 - 10.6 µm, DC - 100 MHz BW, 1 mm2, 100 - 120 or 220 - 240 VAC,” www.thorlabs.com. https://www.thorlabs.com/thorproduct.cfm?partnumber=PDAVJ10 (accessed Jun. 14, 2023).

[20] E. Smith and G. Zummo, Eds., Characterization of Infrared Detectors. 2014.

[21] “Barium Fluoride (BaF2) Lenses,” Barium Fluoride (BaF2) Lenses — EKSMA Optics, https://eksmaoptics.com/optical-components/uv-and-ir-optics/barium-fluoride-baf2-lenses/ (accessed Jun. 9, 2023).

[22] S. Reifel, “Stan-Reifel/Speedystepper: Stepper Motor Control Library for Arduino,” GitHub, https://github.com/Stan-Reifel/SpeedyStepper (accessed Jun. 9, 2023).

[23] P. stoffregen, “Teensy 4.0,” www.pjrc.com. https://www.pjrc.com/store/teensy40.html (accessed Jun. 09, 2023).

[24] Earnest Yen T.T.A., High-Q Aluminum Nitride RF MEMS Lamb Wave Resonators and Narrowband Filters. University of California, Berkeley. (2012).

[25] J. Koo, A. Tazzoli, J. Segovia-Fernandez, G. Piazza and B. Otis, ”A 173 dBc/Hz at 1 MHz offset Colpitts oscillator using AlN contour-mode MEMS resonator,” Proceedings of the IEEE 2013 Custom Integrated Circuits Conference, San Jose, CA, USA, 2013, doi: 10.1109/CICC.2013.6658547.

[26] Y. Hui, S. Kang, Z. Qian and M. Rinaldi, ”Uncooled Infrared Detector Based on an Aluminum Nitride Piezoelectric Fishnet Metasurface,” in Journal of Microelectromechanical Systems, vol. 30, no. 1, pp. 165-172, Feb. 2021, doi: 10.1109/JMEMS.2020.3040953.

[27] Jozef Franciszek Piotrowski, Antoni Rogalski, ”High-Operating-Temperature Infrared Photodetectors.” SPIE digital library, doi.org/10.1117/3.717228.

[28] Discussion about Noise Equivalent Power and its use for photon noise calculation, Samuel Leclercq, 2007

[29] D. B. Leeson, ”A simple model of feedback oscillator noise spectrum,” in Proceedings of the IEEE, vol. 54, no. 2, pp. 329-330, Feb. 1966, doi: 10.1109/PROC.1966.4682.

[30] Zhu, Haoshen & Lee, Joshua E-Y. (2015). AlN Piezoelectric on Silicon MEMS Resonator with Boosted Q using Planar Patterned Phononic Crystals on Anchors. Proceedings of the IEEE International Conference on Micro Electro Mechanical Systems (MEMS). 2015. 10.1109/MEMSYS.2015.7051079.

[31] X. Wu, F. Bao, X. Zhou, Q. Wu, J. Liu and J. Bao, ”Spider Web-Shaped Phononic Crystals for Quality Factor Improvement of Piezoelectric-on-Silicon MEMS resonators,” 2019 IEEE International Ultrasonics Symposium (IUS), Glasgow, UK, 2019, pp. 1724-1726, doi: 10.1109/ULTSYM.2019.8926212.

[32] Li L, He W, Tong Z, Liu H, Xie M. Q-Factor Enhancement of Coupling Bragg and Local Resonance Band Gaps in Single-Phase Phononic Crystals for TPOS MEMS Resonator. Micromachines (Basel). 2022 Jul 29;13(8):1217. doi: 10.3390/mi13081217. PMID: 36014140; PMCID: PMC9415325.

[33] Haoshen Zhu, Joshua E.-Y. Lee,Design of Phononic Crystal Tethers for Frequency-selective Quality Factor Enhancement in AlN Piezoelectric-on-silicon Resonators,Procedia Engineering,Volume 120,2015,Pages 516-519,ISSN 1877-7058,https://doi.org/10.1016/j.proeng.2015.08.689.

Appendix

The Copper Mountain Tech. TR1300/1 VNA offers a helpful programming guide with examples. Below is the Matlab code used to command and read data from the VNA.

```
vna = tcpclient("127.0.0.1", 5025, "Timeout",
    20, "ConnectTimeout", 5);
write(vna, [uint8('TRIG:SOUR BUS'), 0x0A]);%
    Set VNA trigger to BUS trigger
write(vna, [uint8('*OPC?'), nl]);
opc_response = VNAread(vna);
write(vna, [uint8('TRIG:SING'), nl]);
write(vna, [uint8('*OPC?'), nl]);
opc_response = VNAread(vna);
write(vna, [uint8('SENSe1:FREQuency:DATA?'),
    nl]);
Freq = VNAread(vna);
write(vna, [uint8('*OPC?'), nl]);
opc_response = VNAread(vna);
Freq = char(Freq);
Freq = str2num(Freq);
% Read measurement data into array
write(vna, [uint8('CALC1:DATA:FDAT?'), nl]);
data = VNAread(vna);
data = char(data);
data = str2num(data);
data = data(1:2:end); % skip every other
    element in the array
% -= measurement complete =-
function query_response = VNAread(app_vna)
query_response = '';
   while true
      partial_query_response = read(app_vna);
      if(isempty(partial_query_response)~=1)
         last_index =
             length(partial_query_response);
         query_response =
             strcat(query_response,
             partial_query_response);
         if
             (partial_query_response(last_index)
             == 10) % 10 is newline
            break;
         end
      end
   end
end
```

The algorithm demonstrates the way that each device is found and measured.

```
for Sy=1:7
   for Sx=1:3
      x=xc+sum(dx(1:3));y=yc;
      for xi=1:15
         for yi=1:9
            dev_name=chip+sprintf('-%d%d-%d%d',
                Sx, Sy, xi, yi)
```

```
            moveStage(stage, x, y)
            probeDown(MCU)
            VNAmeasurement(vna, dev_name)
            probeUp(MCU)
            y=y+dy;
        end
        y=yc; x=x+dx(xi);
    end
    xc=xc+dxc;
  end
  xc=0; yc=yc+dyc;
end
```

For full access to the code for automation, interfacing, and data analysis please see this github publication: ryan6026/AutomaticProbeStation

ACKNOWLEDGMENT

The author would like to thank Juan Sebastian Gomez-Diaz for his mentorship and support, as well as Diego Yankelevich, and William Putnam. Additionally the author extends a special thanks to Jeronimo Segovia-Fernandez, Earnest Yen, and the rest of the TI team. A big thanks to Melissa Gulseren and Mathew Benson for their help on the project as well.